ADVANCED MATERIALS
www.advmat.de

Phase Pure 2D Perovskite for High-Performance 2D–3D Heterostructured Perovskite Solar Cells

Pengwei Li, Yiqiang Zhang, Chao Liang, Guichuan Xing, Xiaolong Liu, Fengyu Li, Xiaotao Liu, Xiaotian Hu, Guosheng Shao, and Yanlin Song**

Three-dimensional (3D) metal-halide perovskite solar cells (PSCs) have demonstrated exceptional high efficiency. However, instability of the 3D perovskite is the main challenge for industrialization. Incorporation of some long organic cations into perovskite crystal to terminate the lattice, and function as moisture and oxygen passivation layer and ion migration blocking layer, is proven to be an effective method to enhance the perovskite stability. Unfortunately, this method typically sacrifices charge-carrier extraction efficiency of the perovskites. Even in 2D–3D vertically aligned heterostructures, a spread of bandgaps in the 2D due to varying degrees of quantum confinement also results in charge-carrier localization and carrier mobility reduction. A trade-off between the power conversion efficiency and stability is made. Here, by introducing 2D $C_6H_{18}N_2O_2PbI_4$ ($EDBEPbI_4$) microcrystals into the precursor solution, the grain boundaries of the deposited 3D perovskite film are vertically passivated with phase pure 2D perovskite. The phases pure (inorganic layer number $n = 1$) 2D perovskite can minimize photogenerated charge-carrier localization in the low-dimensional perovskite. The dominant vertical alignment does not affect charge-carrier extraction. Therefore, high-efficiency (21.06%) and ultrastable (retain 90% of the initial efficiency after 3000 h in air) planar PSCs are demonstrated with these 2D–3D mixtures.

Organic–inorganic metal halide perovskites are the most promising next-generation photovoltaic materials with remarkable optoelectronic properties, such as large photon absorption coefficient, long-range balanced charge-carrier diffusion lengths, low density of deep trap states, high charge-carrier mobility, and efficient photo-generated exciton dissociation.[1–5] Tremendous efforts have been devoted to propel the certified power conversion efficiency (PCE) of perovskite solar cells (PSCs) over 23%, which is comparable or even higher than that of polycrystalline silicon solar cells.[6,7] However, up to now, the instability of metal-halide perovskites seriously hinders the optoelectronic devices' long-term performance under ambient operation conditions.[8,9] The small organic cations and halogen ions will migrate inside the three-dimensional (3D) perovskite crystals under electric and/or optoelectrical fields. The perovskite crystals could also be decomposed back into the precursors by moisture, oxygen, heat, electric field, and ultraviolet exposure.[10–13] Despite many efforts from multiple research groups have been made to improve the stability,[14–17] the low formation energy and its pronounced hydroscopic nature of 3D perovskites are still not ameliorated.[18,19] In these circumstances, introducing some long organic cations into the perovskite crystal to terminate the lattice, function as moisture and oxygen passivation layer and ion migration blocking layer, has been proven to be an effective method to enhance the perovskite stability.[20,21]

Depending on the introduced long cation composition, percentage and processing procedures, the perovskite crystallinity could be reduced from 3D to quasi-two-dimensional (2D). 2D perovskites take the generic structural formula of

P. W. Li, Prof. F. Y. Li, X. T. Hu, Prof. Y. L. Song
Key Laboratory of Green Printing CAS Research/Education Center for Excellence in Molecular Sciences Institute of Chemistry
Chinese Academy of Sciences (ICCAS)
Beijing Engineering Research Center of Nanomaterials for Green Printing Technology
National Laboratory for Molecular Sciences (BNLMS)
Beijing 100190, P. R. China
E-mail: ylsong@iccas.ac.cn
P. W. Li, X. L. Liu, X. T. Hu
University of Chinese Academy of Sciences
Beijing 100049, P. R. China
Prof. Y. Q. Zhang, X. T. Liu, Prof. G. S. Shao
State Centre for International Cooperation on Designer Low-Carbon and Environmental Material (SCICDLCEM)
School of Materials Science and Engineering
ZhengZhou University
ZhengZhou 450001, P. R. China
C. Liang, Prof. G. C. Xing
Joint Key Laboratory of the Ministry of Education
Institute of Applied Physics and Materials Engineering
University of Macau
Avenida da Universidade
Taipa, Macau 999078, P. R. China
E-mail: gcxing@umac.mo
The ORCID identification number(s) for the author(s) of this article can be found under https://doi.org/10.1002/adma.201805323.

DOI: 10.1002/adma.201805323

$(RNH_3)_2A_{n-1}M_nX_{3n+1}$ (n = 1, 2, 3, 4,...), where RNH_3 is a primary aliphatic or aromatic alkylammonium cation, A is monovalent organic cation, M is a divalent metal, and X is a halide anion.[22,23] Compared with 3D perovskites, 2D layered perovskites possess much larger formation energy, superior moisture stability, larger degrees of freedom in chemistry components and can effectively suppress ion migration.[24,25] Therefore, solar cells based on the 2D perovskites had been proven to improve device stability. For example, phenyl ethylammonium was first used as a large organic cation for improving the device stability.[20] Subsequently, Kanatzidis and co-workers introduced butyl ammonium (BA) as the barrier into the perovskite crystal and obtained stable solar cells with decent PCE of 4.02% by tuning the 2D inorganic layer numbers.[21] Furthermore, Tsai et al. adopted a hot casting approach to control the alignment of the 2D perovskite layers perpendicular to the substrate and demonstrated high-efficiency (12.5%) solar cell with improved moisture and light stability.[26] Recently, the PCE of the 2D perovskite PSC is further improved to 13.7% via cesium doping.[27] Despite the significantly improved stability, the photovoltaic performance of 2D perovskites in PSCs is restricted by their quantum confinement, low carrier mobility, high dielectric constant, and narrower absorption windows.[21–23,25]

The 2D–3D mixtures seemed could inherit the good stability from 2D perovskite and the excellent optoelectronic properties from 3D perovskite. The solar cells based on these mixtures showed enhanced stability with improved PCE. In 2017, Nazeeruddin et al. demonstrated 14.6% (PCE) device with one year stability based on gradually organized 2D–3D $(HOOC(CH_2)_4NH_3)_2PbI_4/CH_3NH_3PbI_3$ mixtures.[28] In the same year, with the BA incorporated mixed-cation lead mixed-halide 2D–3D superlattice, Snaith and co-workers realized solar cells with PCE over 20% and stability over 1000 h in air.[29] However, up to now, the devices with 2D–3D mixture still need to sacrifice part of the charge-carrier extraction efficiency compared to the one with 3D perovskites. The 2D perovskites are typically self-assembled in multiple quantum wells (MQWs).[30–34] A spread of bandgaps due to varying degree of quantum confinement will result in charge-carrier localization and carrier mobility reduction.[35] The horizontally layered 2D perovskites will also function as the charge-carrier extraction barrier layers to the electrodes. Therefore, a trade-off between the PCE and stability has to be made.

Herein, we incorporated long-chain $EDBEPbI_4$ (EDBE = 2,2-(ethylenedioxy)bis(ethylammonium)) into 3D perovskites to form a new phase-segregated vertical heterojunction (PVHH) of 2D–3D perovskite. The 3D perovskite crystal grain boundaries (GBs) are vertically passivated with phase pure 2D perovskite in the solution processed films. The phase pure (inorganic layer number n = 1) 2D perovskite could minimize photo-generated charge-carrier localization in the low-dimensional perovskites. The dominant vertical alignment would not affect the charge-carrier extraction from 3D perovskite to the electrodes. Therefore, the trade-off between PCE and stability could be overcome by using this 2D–3D PVHH. In detail, due to passivation by the 2D perovskite, the trap density is largely reduced from 10^{15} cm^{-3} in 3D perovskite to 10^{14} cm^{-3} in 2D–3D PVHH. The grain size, carrier lifetime, and carrier vertical diffusion lengths of the 3D perovskite are greatly enhanced in the 2D–3D mixtures. With these innovative structures, we achieved a champion efficiency of 21.06% and a stabilized efficiency of 19.66% in complete solar cells. To demonstrate the up-scale potential of these mixtures, solar modules (PCE ≈11.59%) with active area of 342 cm^2 were fabricated with a printing method. These modules could sustain 90% of the original efficiency after three months (over 3000 h) in air.

Synthetic chemistry provides powerful tools to control the perovskite structural properties.[36,37] To enable quantitative analysis of the crystal structure, we synthesized $EDBEPbI_4$ 2D microcrystals (Figure S1, Supporting Information) from solution with precursors of EDBE and lead iodide (see Experimental Section for details, Supporting Information). High-quality single crystals were selected for crystal structure analysis (see Table S1 and CIF for details, Supporting Information). $EDBEPbI_4$ microcrystals belongs to the monoclinic $P2_1/a$ space group with lattice parameters of a = 6.5266 (9) Å, b = 29.484 (4) Å, c = 9.3071 (13) Å, and β = 91.563 (2)°(Figure S2, Supporting Information), which correspond well to the literature.[38] The X-ray diffraction (XRD) pattern (Figure S3, Supporting Information) shows a peak located at $2\theta < 10°$, which is a characteristic feature of 2D perovskite. In addition, the absorption peak located at 480 nm (Figure S4, Supporting Information) indicates that $(EDBE)PbI_4$ is a wide-bandgap semiconductor.

The schematic structure of 2D layers interspersed 3D perovskite PVHH is shown in **Figure 1**a. The samples were prepared by mixing the 2D $EDBEPbI_4$ microcrystals with 3D perovskite ($MAPbI_3$) precursors in solution with different molar ratios $(EDBEPbI_4)_x(MAPbI_3)_{1-x}$. The color of the blended solution deepens as the 2D perovskite content increases and no clear 2D excitonic absorption peak around 480 nm is observed (Figure S5, Supporting Information), which indicate that the 2D crystals are well dissolved and dispersed in the solution. To determine the phase of the films deposited from these solutions, XRD patterns were recorded and shown in Figure 1b. The results clearly show that all samples could be indexed to the 3D perovskite phase within the low 2D doping concentration ($x \leq 0.05$). However, with 2D crystals in the precursor solution, there is a new peak emerged at the small diffraction angle ($2\theta < 10°$). This new XRD peak corresponds well to the 2D EDBEPbI4 phase (Figure S3, Supporting Information). It suggests that the long cations are incorporated into the crystals by dominantly forming phase pure 2D thin layers (n = 1) rather than MQWs. The linear absorption spectra further confirmed this conclusion. As shown in Figure 1c, the absorption spectra of the films deposited from the mixtures are dominated by the features originated from 3D $MAPbI_3$ with an additional sharp peak located at 480 nm. These peak increases while increasing the 2D crystal content in precursor solution and are closely matched with the excitonic absorption of phase pure 2D thin layers (n = 1).

To further explore the surface topography, perovskite films were fabricated via one-step spin coating on the SnO_2 films followed by a slow drying process (see Experimental Section for details, Supporting Information). Then scanning electron microscopy (SEM) was conducted and the images of these films are shown in Figure 1d–g. These results clearly show that all the films possess a compact, pinhole-free morphology. While with suitable amount (x = 0.01 and 0.03) 2D doping, some "flake-like"

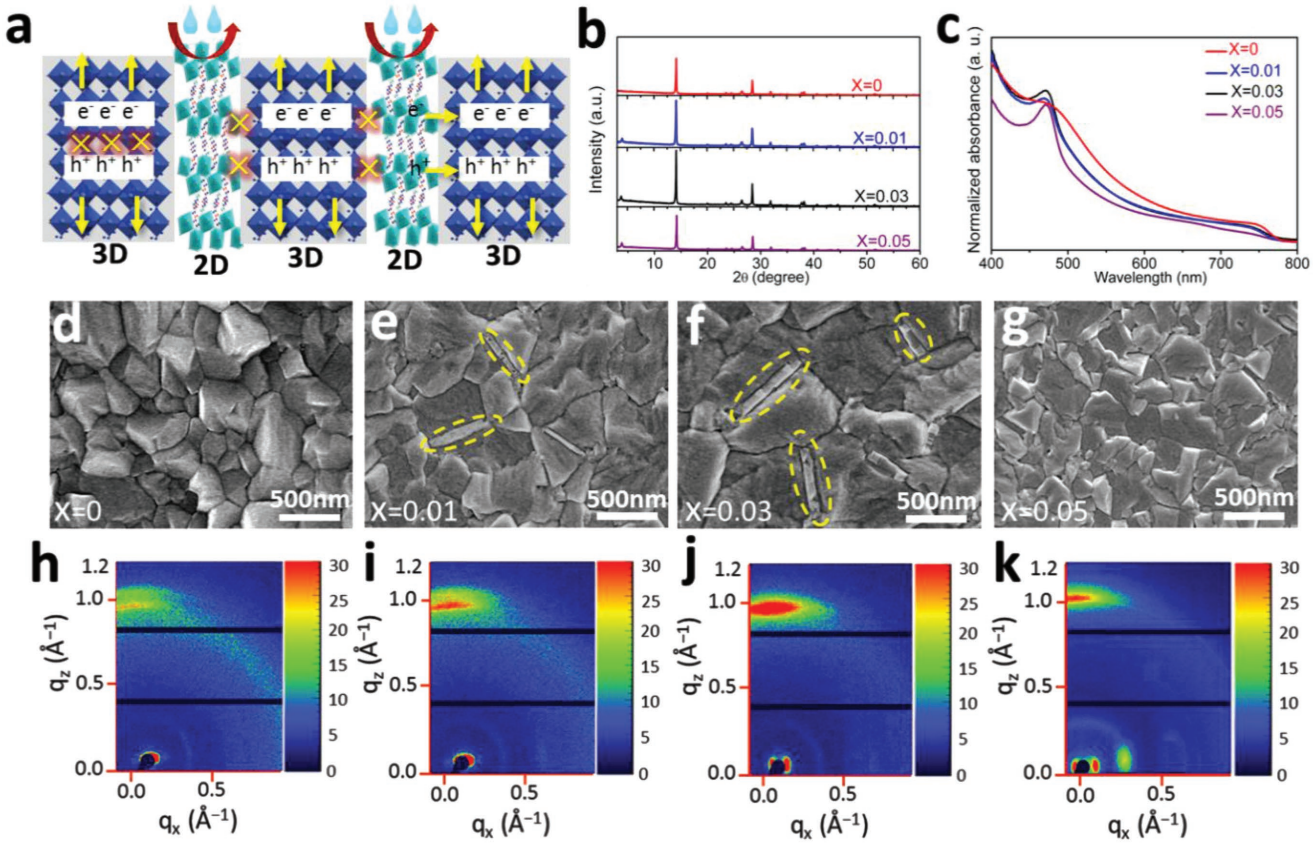

Figure 1. Structural characterization and morphology. a) Schematic illustration of 2D–3D PVHH structure. b) 2D perovskite doping concentration dependent XRD patterns and c) UV–vis absorption spectra of the $(EDBEPbI_4)_x(MAPbI_3)_{1-x}$ films. d–g) SEM images of perovskite films with different 2D concentrations. The "flake-like" structure in the yellow area is $EDBEPbI_4$. h–k) GIWAXS images of the films with different 2D concentrations. Reflections at $q_z \approx 1$ is assigned to 3D perovskite (110).

crystallites vertically lie between the 3D grains (Figure 1e,f). These vertically aligned "flake-like" crystallites are attributed to the 2D $EDBEPbI_4$ perovskites. The vertical alignment could be induced by the exposed amine groups at the two faces of 2D $EDBEPbI_4$ perovskite can effectively interact with the 3D perovskite, resulting in the 2D $EDBEPbI_4$ perovskite prefers to grow vertically between the 3D perovskite grains.[39,40] Photoluminescence (PL) color micro images further verified the presence of 2D perovskite between the 3D grains (Figure S6, Supporting Information). The SEM images and analyses (Figure 1d–g) also clearly show that the average size of the 3D grains is almost increased by two times with suitable amount 2D doping (Figure S7, Supporting Information). This enlarged crystal size may be caused by the slowed crystallization due to that the amino group at the ends of diamine organic ligands were coordinated to the 3D perovskite.[41,42] The surface flatness of the film is also improved by the 2D perovskite doping (Figure S8, Supporting Information). However, if the 2D doping concentration was further increased to $x = 0.05$, a very different surface topography is observed. The "flake-like" structures are becoming blurred, which is attributed to a high density of 2D perovskite creeps out of GBs to the surface of 3D perovskite grains.[29] Excessive 2D perovskites will also impede the growth of large 3D perovskite grains (Figure S7d, Supporting Information).

The crystal orientations of the deposited films were further examined by the Grazing-incidence wide-angle X-ray scattering (GIWAXS) measurements. The results are shown in Figure 1h–k. The pure ($x = 0$) 3D perovskite film exhibits clear reflection ring with strong intensity along certain extended arc segments, which indicates the 3D $MAPbI_3$ is crystalized with not much preference of orientation.[29] When suitable amount 2D $EDBEPbI_4$ ($x = 0.01$ and 0.03) was incorporated, the (*hk0*) reflection peak intensity is greatly enhanced and the powder diffraction ring is weakened. These results indicate that the 3D perovskite prefers to crystalize parallel to the substrate in [110] face with the assistance of 2D perovskite in the precursor solution. The better crystallinity of the 2D–3D mixture ($x = 0.03$) is also evidenced as clearer crystal lattice phonon features than that of the pure 3D counterpart (Figure S9, Supporting Information). However, when the 2D doping concentration was further increased, a new reflection peak arises ($x = 0.05$, Figure 1k). This peak could not be attributed to 3D perovskite since it is too low in 2θ. Therefore, this new peak is attributed to the 2D perovskite layers with larger *d*-spacing than the 3D perovskite.[29] These 2D perovskite layers may arise from a high density of the 2D perovskite creep out of GBs to the surface of 3D perovskite grains.

Incorporating some long cations into 3D perovskite precursor solution, the perovskite MQWs with a spread of

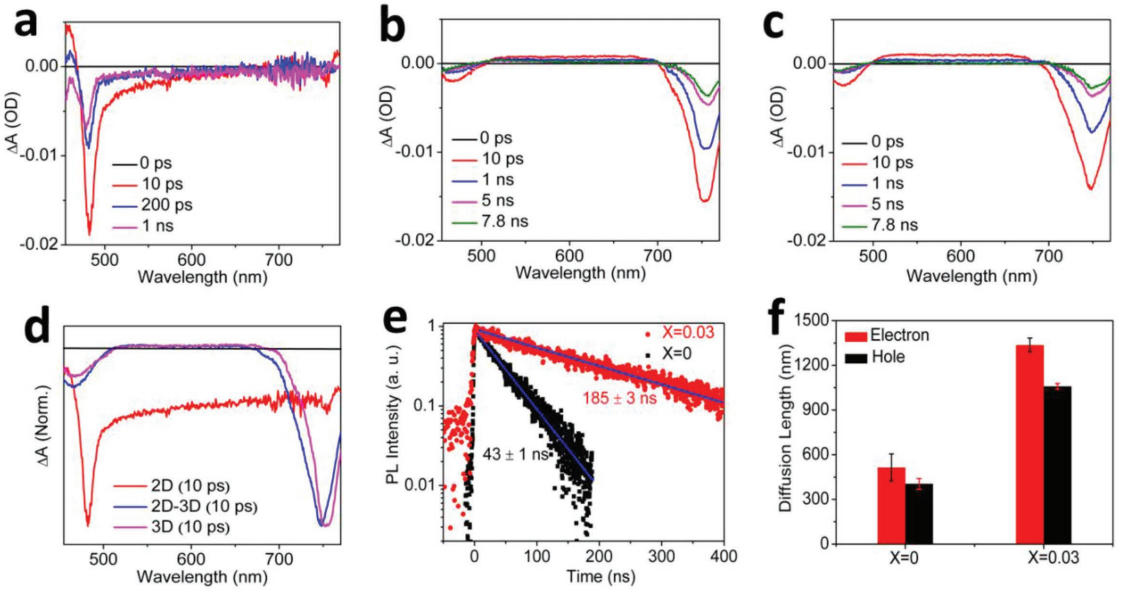

Figure 2. TAS and carrier diffusion length. a–c) TA spectra for $x = 1$ (pure 2D perovskite), $x = 0$ (pure 3D perovskite), and $x = 0.03$ (2D–3D heterostructure) films after excitation at 425 nm (1 kHz, 150 fs, and 13 mJ cm^{-2}) with delay time of 0–7.8 ps. d) Normalized TA spectra at 10 ps delay for comparison. e) TRPL decay transients measured at 766 ± 20 nm for $x = 0$ and 0.03 films on quartz. f) Extracted hole and electron diffusion lengths for $x = 0$ and 0.03 films.

inorganic layer numbers are typically formed.[30–33] These MQWs will result in charge-carrier localization and carrier mobility reduction.[34] In this work, by mixing the 2D (EDBE)PbI_4 microcrystals with 3D $MAPbI_3$ precursors in solution, the XRD and linear absorption results have suggested that the deposited 2D–3D heterojunction with near phase pure 2D ($n = 1$) perovskite could be obtained. To further verify the phase purity of 2D perovskite in the heterojunction, femtosecond transient absorption spectroscopies (TAS) of these films were collected. Since at the early delay times without being submerged by the continuum transitions, the presence of MQWs with different n values could be easily resolved by probing the corresponding excitonic resonances. The TA spectra at various delay times for the 2D, 3D, and 2D–3D mixed ($x = 0.03$) perovskites are shown in **Figure 2**a–c. The negative TA peaks represent bleached excitonic transitions. The pure 2D perovskite film (Figure 2a) features only one bleaching peak at ≈480 nm, which corresponds to the exciton transition in (EDBE)PbI_4 ($n = 1$). The pure 3D perovskite film (Figure 2b) features two bleaching peaks at 480 and 760 nm, which could be attributed to transitions associated with high energy states and band edge states, respectively.[40] Surprisingly, the 2D–3D mixed perovskite film (Figure 2c) shows very similar TA spectra features as that of the pure 3D perovskite film does. Only the two bleaching peaks located at 480 and 760 nm are observed and the relative amplitude ratio of 480–760 nm is slightly increased in the mixed perovskite (Figure 2d). No other small amplitudes for lower n ($n \geq 2$) QWs could be clearly resolved, which is in sharp contrast to the TA spectrum features observed for perovskite MQWs.[33] These results further confirmed that the long cations are incorporated by dominantly forming phase pure 2D thin layers ($n = 1$) rather than MQWs.

To further explore whether the excellent charge-carrier transportation and extraction in 3D perovskite will be sacrificed by forming this 2D–3D PVHH, PL quenching method was used to determine these properties. The photoexcited electron and hole dynamics in 2D–3D PVHH and pure 3D perovskite were systematically investigated through time-resolved PL (TRPL) spectroscopy of bare perovskite films and heterojunctions with electron and hole extraction materials. Here, the 2,2,7,7-tetrakis[N,N-di(4-methoxyphenyl)amino]-9,9-spirobifluorene (Spiro-OMeTAD) and [6,6]-phenyl-C61-butyric acid methyl ester (PCBM) with suitable valence band and conduction band levels were used as the hole and electron extractor, respectively. The results clearly show that the carrier lifetime of 185 ± 3 ns for 2D–3D PVHH is much longer than that of the pure 3D counterpart (43 ± 1 ns) (Figure 2e), which demonstrates again the high crystal quality of the 2D–3D PVHH. The PL lifetimes were greatly shortened when the 2D–3D PVHH layers were interfaced with the Spiro-OMeTAD and PCBM, with fitted lifetimes of 5.2 ± 0.1 and 3.3 ± 0.1 ns, as compared to 7.1 ± 0.1 and 4.7 ± 0.2 ns for the pure 3D perovskites, respectively (Figure S10, Supporting Information). Therefore, the charge-carrier transfer times (τ_{CT}) could be estimated to be several nanoseconds for both the 2D–3D PVHH and 3D perovskites by using the equation of $1/\tau_{Heterojunction} = 1/\tau_{Perovskite} + 1/\tau_{CT}$. However, the estimated charge extraction efficiencies (over 97%) for the 2D–3D PVHH are much larger than that (less than 84%) for the 3D counterpart. Following the analytical solutions to the 1D diffusion equations, the carrier diffusion length (L_D) could be expressed as[43,44]:

$$L_D \approx \frac{2d}{\pi}\sqrt{2\left(\frac{\tau}{\tau_{quench}} - 1\right)} \quad (1)$$

where d is thickness of the perovskite film, τ is the carrier lifetime, and τ_{quench} is quenched lifetime of electrons or holes. With the above experimental results, the calculated diffusion

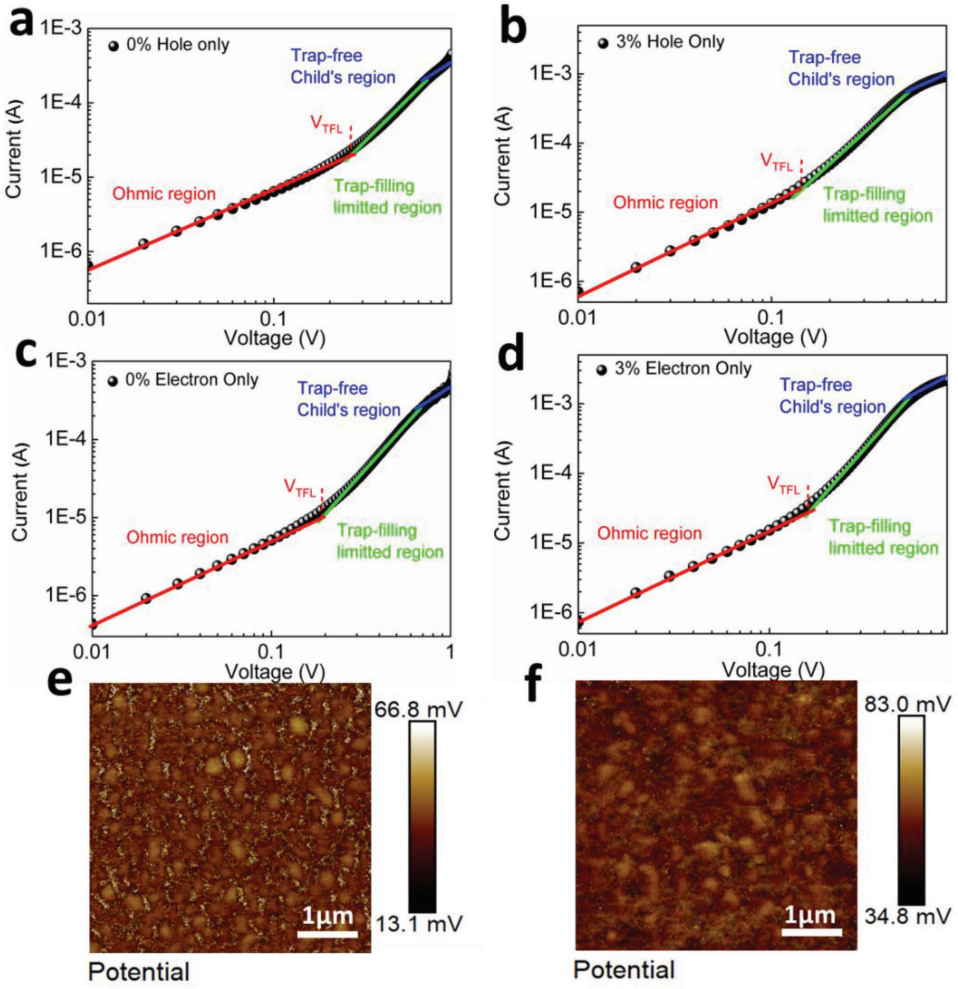

Figure 3. Characterization of carrier mobility, trap density and SP. a,b) Current–voltage curve for a hole-only device (glass/ITO/PEDOT:PSS/perovskite/Spiro-OMeTAD/Au). c,d) Current–voltage curve for an electron-only device (glass/FTO/TiO_2/perovskite/PCBM/Ag). e,f) SP of x = 0 and 0.03 films via using a Park Systems XE100 AFM system with an AC voltage of ≈2 V.

lengths are shown in Figure 2f. It clearly shows that both of the electron and hole diffusion lengths of the 2D–3D PVHH are near three times longer than that of the 3D $MAPbI_3$. These results indicate that the charge-carrier transportation and extraction could be enhanced, rather than reduced by incorporating the long cations into the crystal to form such 2D–3D PVHH.

The influences of long cation incorporation on trap density and charge mobility were examined with the space-charge-limited current (SCLC) measurements, which were performed on both 2D–3D PVHH and 3D perovskites with configurations of electron-only and hole-only devices. The trap density (N_t) is determined by the trap-filled limit voltage based on the following equation:[45]

$$N_t = \frac{2V_{TFL}\varepsilon_r\varepsilon_0}{qL^2} \quad (2)$$

where V_{TFL} is onset voltage of the trap-filled limit region, L is thickness of the perovskite film, ε_r (= 32) is relative dielectric constant of $MAPbI_3$,[45] and ε_0 is the vacuum permittivity. As shown in **Figure 3**a,b, the hole trap densities are estimated to be 6.2 ± 0.5 × 10^{15} and 2.8 ± 0.3 × 10^{14} cm^{-3} for the pure 3D (x = 0) and 2D–3D PVHH (x = 0.03) perovskite films, respectively. Similarly, the corresponding electron trap densities are estimated to be 4.4 ± 0.5 × 10^{15} and 2.9 ± 0.3 × 10^{14} cm^{-3} (Figure 3c,d). Here, we would like to mention that such kinds of measurements are typically complicated by ionic motion in metal-halide perovskite. However, due to the 3D perovskite grains are effectively passivated by the 2D perovskite, the ionic motion and J–V hysteresis could be largely reduced in the 2D–3D PVHH. Therefore, the trap densities estimated for the 2D–3D PVHH should be in the reasonable range. The estimated results clearly show that the trap densities are greatly reduced by incorporating suitable amount long cations into the crystal to form such 2D–3D PVHH. These reduced trap densities are consistent with the enlarged 3D perovskite grain size and GB passivation with the 2D perovskite in 2D–3D PVHH (x = 0.03) (Figure 1f). When operating in the trap-free SCLC regime, the dark current of the devices could be well fitted (blue line in Figure 3a–d) by the Mott–Gurney law:

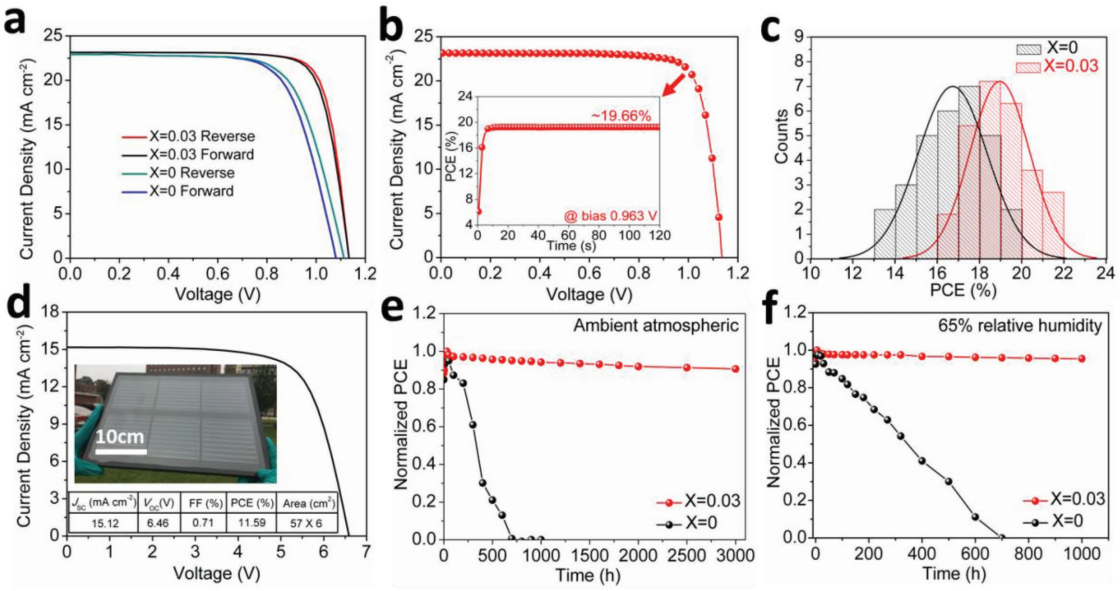

Figure 4. Performance of the 2D–3D PSCs. a) Hysteresis analysis of the PSCs employing $Cs_{0.05}(FA_{0.83}MA_{0.17})_{0.95}Pb(I_{0.83}Br_{0.17})_3$ (x = 0) and $(EDBEPbI_4)_{0.03}[Cs_{0.05}(FA_{0.83}MA_{0.17})_{0.95}Pb(I_{0.83}Br_{0.17})_3]_{0.97}$ (x = 0.03) with a scan rate of 25 mV s^{-1}. b) J–V characteristic of the champion PSC based on x = 0.03 perovskite and the inset shows the corresponding SSE. c) Histogram of the number of cells as a function of PCE of x = 0 and 0.03 devices. d) J–V characteristic of a champion module. Inset is photograph of the module with active area 342 cm^2. The module was simply encapsulated to avoid mechanical damages and stored under dark condition. e,f) The module stability were tested under ambient atmospheric conditions (e) and at 65% relative humidity (f).

$$J_D = \frac{9\mu\varepsilon_r\varepsilon_0 V_b^2}{8L^3} \tag{3}$$

where V_b is applied voltage. From curve fittings (Figure 3a–d), the electron and hole mobilities are extracted as $2.55 \pm 1.1 \times 10^{-2}$ and $2.05 \pm 1.8 \times 10^{-2}$ cm^2 V^{-1} s^{-1} for the 3D perovskite, $1.18 \pm 1.3 \times 10^{-1}$ and $9.22 \pm 2.1 \times 10^{-2}$ cm^2 V^{-1} s^{-1} for the 2D–3D PVHH (x = 0.03), respectively. These results further confirmed that the charge-carrier transportation could be enhanced, rather than reduced by incorporating suitable amount long cations into the crystal to form such 2D–3D PVHH.

Scanning Kelvin probe microscopy was used to investigate surface potential (SP) of the 3D and 2D–3D PVHH (x = 0.03) perovskite films. As shown in Figure 3e,f, the two films have distinctly different SP patterns. The 3D perovskite film demonstrates higher SP at the GBs than that of the grain interior, indicating a downward band bending at the GBs which will cause electron trapping.[46] Obviously, the SP difference between GB and interior is slashed in the whole 2D–3D PVHH film, resulting in negligible band bending at GBs. The near homogeneously SP for all the 3D perovskite grains indicates that almost all the 3D perovskite GBs are passivated with the 2D perovskite layers, though part of them may be too thin to be detected with SEM. These results further confirmed passivation of the 3D perovskite with the 2D $EDBEPbI_4$ and offered the reason for the longer carrier lifetime observed in the 2D–3D PVHH (Figure 2e). Furthermore, the average SP of the 3D film is weaker than that of the 2D–3D film, which suggests a larger downward surface band-bending for the mixed perovskite film. The larger downward surface band bending is in favor of charge-carrier separation and will result in higher fill factor (FF), current density (J_{SC}), and reduced hysteresis in the cells.

To demonstrate the outstanding performance of 2D–3D PVHH perovskite in photovoltaics, solar cells with n–i–p planar heterojunction architecture (glass/FTO/SnO_2/perovskite/Spiro-OMeTAD/Au) were fabricated. The performance was evaluated by measuring their photocurrent density versus voltage (J–V) curves (Figure S11, Supporting Information). The 2D–3D ($MAPbI_3$) PVHH perovskite with x = 0.03 shows the highest PCE of 19.13%, while PCEs of the devices with other perovskite compositions are 18.67% (x = 0.01), 18.05% (x = 0) and 16.96% (x = 0.05), respectively (Table S2, Supporting Information). The mixed cation (FA, MA, and Cs) PSCs have been widely recognized with improved device performance. To examine whether the introduced 2D $(EDBE)PbI_4$ have the same effect on mixed cation (FA, MA, and Cs) PSCs, we mixed the 2D $(EDBE)PbI_4$ microcrystals into 3D $(Cs_{0.05}(FA_{0.83}MA_{0.17})_{0.95}Pb(I_{0.83}Br_{0.17})_3)$ perovskite precursors for fabricating PSCs. **Figure 4**a shows J–V characteristics of the devices (x = 0 and 0.03) and the performance parameters are summarized in Table 1. Clearly, the control device (x = 0) exhibits significant J–V hysteresis, while the hysteresis of x = 0.03 device is almost negligible. This could be attributed to the reduced trap density and improved charge-carrier transportation and extraction in the 2D–3D PVHH (x = 0.03) perovskite (Figure S12, Supporting Information). In addition, the x = 0.03 device exhibits higher incident photon-to-current efficiency than the control device does (Figure S13, Supporting Information), yielding integrated J_{SC} value of 22. and 22.36 mA cm^{-2} respectively, which are in good agreement with the J–V curves (Figure 4a). Finally, the champion device delivers an open-circuit voltage of 1.13 V, a short-circuit current (J_{SC}) of 23.53 mA cm^{-2}, an FF of 79.2%, and a PCE of

Table 1. PCSs performance parameters with $x = 0$ and 0.03 based devices.

	J_{SC} [mA cm^{-2}]	V_{OC} [V]	FF [%]	PCE [%]
Device ($x = 0$)				
Forward	23.05	1.03	67.6	16.04
Reverse	23.06	1.08	72.5	18.05
Champion	23.17	1.11	73.9	19.01
Average	22.81 ± 0.8	1.07 ± 0.03	68.02 ± 5.4	16.59 ± 1.12
Device ($x = 0.03$)				
Forward	23.31	1.12	77.3	20.18
Reverse	23.31	1.12	77.6	20.25
Champion	23.53	1.13	79.2	21.06
Average	23.21 ± 0.6	1.11 ± 0.03	75.1 ± 4.2	19.09 ± 0.92

21.06% under reverse scan with a steady-state efficiency (SSE) of 19.66% (Figure 4b). This is one of the best PCEs achieved among representative 2D–3D perovskite devices (see Table S3 for details, Supporting Information). Contrastively, the control device exhibits a V_{OC} of 1.11 V, a J_{SC} of 23.17 mA cm^{-2}, and an FF 73.9%, yielding a PCE of 19.01% with an SSE of 17.61% (Figure S14, Supporting Information). Furthermore, the 2D–3D-based devices demonstrated considerable reproducibility with an average efficiency of 19.09% ± 0.92% for 30 devices. However, the control devices ($x = 0$) only exhibited an average efficiency of 16.59% ± 1.12%, as illustrated through the statistical PCE distribution presented in Figure 4c, **Table 1**, and Figure S15 in the Supporting Information.

To demonstrate the up-scale potential of this innovative 2D–3D PVHH ($x = 0.03$) perovskite, large area solar cells were fabricated via printing methods with the carbon as the electrode (see Experimental Section for details). The solar module consists of six solar cells with each area of about 10 × 10 cm^2 (active area 57 cm^2) leading to an active area of 342 cm^2 per module. The photovoltaic performances of the module are shown in Figure 4d and Figure S16 in the Supporting Information. The results show that ultrastable high-efficiency (11.59%) solar modules with the largest reported active area could be achieved, which demonstrates the good up-scale potential. The detail parameters of the individual cells in one module are summarized in Table S4 in the Supporting Information. The tiny performance difference between cells further confirmed the excellent reproducibility of the 2D–3D PVHH PSC.

To demonstrate the excellent stability of such 2D–3D PVHH ($x = 0.03$) perovskite, aging test on modules under ambient atmospheric conditions was performed. The results are presented in Figure 4e. It clearly shows that the 2D–3D PVHH perovskite module demonstrates greatly enhanced stability with less than 10% PCE loss over 3000 h in air. The J–V characteristic and other parameters also deliver excellent long-term stability as shown in Figure S17 in the Supporting Information. In sharp contrast with the 2D–3D PVHH perovskite module, the mixed 3D perovskite module shows over 70% PCE loss after 600 h in air. This large stability difference indicates the doped phase pure $EDBEPbI_4$ could function well as the moisture and oxygen passivation layer and ion migration blocking layer. Notably, such stability improvement is achieved without sacrificing the charge-carrier mobility and extraction efficiency of the perovskites. The accelerated aging test on modules at 65% relative humidity was further performed to probe the capability. As shown in Figure 4f, the 2D–3D-based module could retain over 90% of its initial PCE after 1000 h. However, the control module retained only 10% initial PCE after 600h. Furthermore, the 2D–3D PVHH perovskite also shows good stability under continuous operation. As shown in Figure S18 in the Supporting Information, the 2D–3D module kept over 95% of its initial PCE after continuously working at the maximum power point under continuous illumination conditions for 500 h. In light of the recent reports,[24,26–29,47,48] these results confirm that our device is one of the most stable PSC demonstrated with the 2D–3D perovskite heterostructures (Table S5, Supporting Information).

In conclusion, with the innovative 2D-3D PVHH perovskite, the stability of PSC is shown to be greatly enhanced without sacrificing the PCE. By incorporating suitable amount ($x = 0.03$) long-chain 2D $EDBEPbI_4$ microcrystals into 3D perovskite precursors, the 3D perovskite crystal GBs were vertically passivated with phase pure 2D ($n = 1$) perovskite in the solution-processed films. The phase pure 2D perovskite could minimize photo-generated charge-carrier localization in the low-dimensional perovskite. The dominantly vertical alignment would not affect the charge-carrier extraction from the 3D perovskite to the electrodes. Therefore, the carrier lifetime, mobility, and diffusion length are greatly enhanced and the trap density is greatly reduced in this 2D–3D PVHH perovskite. Accordingly, PSCs with PCE of 21.06% in small size and 11.59% in solar modules (342 cm^2) are obtained without hysteresis based on this 2D–3D PVHH. More importantly, these high-efficiency cells demonstrated excellent stability with less than 10% PCE loss after 3000 h in air. Therefore, the traditional constrain of trade-off between the PCE and stability in PSC could be overcome by using this 2D–3D PVHH perovskite.

Supporting Information

Supporting Information is available from the Wiley Online Library or from the author.

Acknowledgements

P. W. Li, Y. Q. Zhang, and C. Liang contributed equally to this work. The authors acknowledge the financial support by the National Nature Science Foundation of China (Grant Nos 21522308, 51773206, 51573192, 51473173, and 21421061), the National Key R&D Program of China (2018YFA0208501, 2016YFB0401603, 2016YFC1100502, and 2016YFB0401100), the "Strategic Priority Research Program" of Chinese Academy of Sciences (Grant No. XDA09020000), and the External Cooperation Program of BIC, Chinese Academy of Sciences (Grant No. 121111KYSB20150022), the Macau Science and Technology Development Fund (FDCT-116/2016/A3, FDCT-091/2017/A2, and FDCT-014/2017/AMJ), Research Grants (SRG2016-00087-FST, MYRG2018-00148-IAPME) from University of Macau, the Natural Science Foundation of China (91733302, 61605073, and 2015CB932200), and the Young 1000 Talents Global Recruitment Program of China.

Conflict of Interest

The authors declare no conflict of interest.

Keywords

2D–3D heterojunctions, carrier dynamics, diffusion length, perovskite solar cells, stability

Received: August 15, 2018
Revised: September 14, 2018
Published online: November 2, 2018

[1] X. Pu, L. X. Li, H. Q. Song, C. H. Du, Z. F. Zhao, C. Y. Jiang, G. Z. Cao, W. G. Hu, Z. L. Wang, *Adv. Mater.* **2015**, *27*, 2472.
[2] S. D. Stranks, G. E. Eperon, G. Grancini, C. Menelaou, M. J. P. Alcocer, T. Leijtens, L. M. Herz, A. Petrozza, H. J. Snaith, *Science* **2013**, *342*, 341.
[3] G. Xing, N. Mathews, S. S. Lim, N. Yantara, X. Liu, D. Sabba, M. Grätzel, S. Mhaisalkar, T. C. Sum, *Nat. Mater.* **2014**, *13*, 476.
[4] G. Hodes, *Science* **2013**, *342*, 317.
[5] W. Nie, H. Tsai, R. Asadpour, J.-C. Blancon, A. J. Neukirch, G. Gupta, J. J. Crochet, M. Chhowalla, S. Tretiak, M. A. Alam, H.-L. Wang, A. D. Mohite, *Science* **2015**, *347*, 522.
[6] N. J. Jeon, H. Na, E. H. Jung, T.-Y. Yang, Y. G. Lee, G. Kim, H.-W. Shin, S. I. Seok, J. Lee, J. Seo, *Nat. Energy* **2018**, *3*, 682.
[7] Best Research-Cell Efficiencies, National Renewable Energy Laboratory, https://www.nrel.gov/pv/assets/images/efficiency-chart.png (accessed: August 2018).
[8] J. H. Kim, P.-W. Liang, S. T. Williams, N. Cho, C.-C. Chueh, M. S. Glaz, D. S. Ginger, A. K.-Y. Jen, *Adv. Mater.* **2015**, *27*, 695.
[9] T. Niu, J. Lu, R. Munir, J. Li, D. Barrit, X. Zhang, H. Hu, Z. Yang, A. Amassian, K. Zhao, S. (F.) Liu, *Adv. Mater.* **2018**, *30*, 1706576.
[10] J. You, L. Meng, T.-B. Song, T.-F. Guo, Y. (M.) Yang, W.-H. Chang, Z. Hong, H. Chen, H. Zhou, Q. Chen, Y. Liu, N. D. Marco, Y. Yang. *Nat. Nanotechnol.* **2016**, *11*, 75.
[11] R. J. Sutton, G. E. Eperon, L. Miranda, E. S. Parrott, B. A. Kamino, J. B. Patel, M. T. Hörantner, M. B. Johnston, A. A. Haghighirad, D. T. Moore, H. J. Snaith, *Adv. Energy Mater.* **2016**, *6*, 1502458.
[12] D. Bryant, N. Aristidou, S. Pont, I. S. Molina, T. Chotchunangatchaval, S. Wheeler, J. R. Durrantab, S. A. Haque, *Energy Environ. Sci.* **2016**, *9*, 1655.
[13] S. S. Reddy, K. Gunasekar, J. H. Heo, S. H. Im, C. S. Kim, D.-H. Kim, J. H. Moon, J. Y. Lee, M. Song, S.-H. Jin, *Adv. Mater.* **2016**, *28*, 686.
[14] F. Bella, G. Griffini, J.-P. Correa-Baena, G. Saracco, M. Grätzel, A. Hagfeldt, S. Turri, C. Gerbaldi, *Science* **2016**, *354*, 203.
[15] H. Zhou, Q. Chen, G. Li, S. Luo, T. Song, H.-S. Duan, Z. Hong, J. You, Y. Liu, Y. Yang. *Science* **2014**, *345*, 542.
[16] M. Saliba, T. Matsui, J.-Y. Seo, K. Domanski, J.-P. Correa-Baena, M. K. Nazeeruddin, S. M. Zakeeruddin, W. Tress, A. Abate, A. Hagfeldt, M. Grätzel, *Energy Environ. Sci.* **2016**, *9*, 1989.
[17] N. J. Jeon, J. H. Noh, W. S. Yang, Y. C. Kim, S. Ryu, J. Seo, S. I. Seok, *Nature* **2015**, *517*, 476.
[18] D. Bi, P. Gao, R. Scopelliti, E. Oveisi, J. Luo, M. Grätzel, A. Hagfeldt, M. K. Nazeeruddin, *Adv. Mater.* **2016**, *28*, 2910.
[19] T. A. Berhe, W.-N. Su, C.-H. Chen, C.-J. Pan, J.-H. Cheng, H.-M. Chen, M.-C. Tsai, L.-Y. Chen, A. A. Dubale, B.-J. Hwang, *Energy Environ. Sci.* **2016**, *9*, 323.
[20] I. C. Smith, E. T. Hoke, D. Solis-Ibarra, M. D. McGehee, H. I. Karunadasa, *Angew. Chem.* **2014**, *126*, 11414.
[21] D. H. Cao, C. C. Stoumpos, O. K. Farha, J. T. Hupp, M. G. Kanatzidis, *J. Am. Chem. Soc.* **2015**, *137*, 7843.
[22] J. Calabrese, N. L. Jones, R. L. Harlow, N. Herron, D. L. Thorn, Y. Wan, *J. Am. Chem. Soc.* **1991**, *113*, 2328.
[23] C. Ma, D. Shen, T.-W. Ng, M.-F. Lo, C.-S. Lee, *Adv. Mater.* **2018**, *30*, 1800710.
[24] L. N. Quan, M. Yuan, R. Comin, O. Voznyy, E. M. Beauregard, S. Hoogland, A. Buin, A. R. Kirmani, K. Zhao, A. Amassian, D. Ha Kim, E. H. Sargent, *J. Am. Chem. Soc.* **2016**, *138*, 2649.
[25] R. L. Milot, R. J. Sutton, G. E. Eperon, A. A. Haghighirad, J. M. Hardigree, L. Miranda, H. J. Snaith, M. B. Johnston, L. M. Herz, *Nano Lett.* **2016**, *16*, 7001.
[26] H. Tsai, W. Nie, J.-C. Blancon, C. C. Stoumpos, R. Asadpour, B. Harutyunyan, A. J. Neukirch, R. Verduzco, J. J. Crochet, S. Tretiak, L. Pedesseau, J. Even, M. A. Alam, G. Gupta, J. Lou, P. M. Ajayan, M. J. Bedzyk, M. G. Kanatzidis, A. D. Mohite, *Nature* **2016**, *536*, 312.
[27] X. Zhang, X. Ren, B. Liu, R. Munir, X. Zhu, D. Yang, J. Li, Y. Liu, D.-M. Smilgies, R. Li, Z. Yang, T. Niu, X. Wang, A. Amassian, K. Zhao, S. (F.) Liu, *Energy Environ. Sci.* **2017**, *10*, 2095.
[28] G. Grancini, C. Roldán-Carmona, I. Zimmermann, E. Mosconi, X. Lee, D. Martineau, S. Narbey, F. Oswald, F. D. Angelis, M. Grätzel, M. K. Nazeeruddin, *Nat. Commun.* **2017**, *8*, 15684.
[29] Z. Wang, Q. Lin, F. P. Chmiel, N. Sakai, L. M. Herz, H. J. Snaith, *Nat. Energy* **2017**, *2*, 17135.
[30] G. Xing, B. Wu, X. Wu, M. Li, B. Du, Q. Wei, J. Guo, E. K. L. Yeow, T. C. Sum, W. Huang, *Nat. Commun.* **2017**, *8*, 14558.
[31] N. Wang, L. Cheng, R. Ge, S. Zhang, Y. Miao, W. Zou, C. Yi, Y. Sun, Y. Cao, R. Yang, Y. Wei, Q. Guo, Y. Ke, M. Yu, Y. Jin, Y. Liu, Q. Ding, D. Di, L. Yang, G. Xing, H. Tian, C. Jin, F. Gao, R. H. Friend, J. Wang, W. Huang, *Nat. Photonics* **2016**, *10*, 699.
[32] H. Tsai, R. Asadpour, J.-C. Blancon, C. C. Stoumpos, J. Even, P. M. Ajayan, M. G. Kanatzidis, M. A. Alam, A. D. Mohite, W. Nie, *Nat. Commun.* **2018**, *9*, 2130.
[33] M. Yuan, L. N. Quan, R. Comin, G. Walters, R. Sabatini, O. Voznyy, S. Hoogland, Y. Zhao, E. M. Beauregard, P. Kanjanaboos, Z. Lu, D. H. Kim, E. H. Sargent, *Nat. Nanotechnol.* **2016**, *11*, 872.
[34] J. Byun, H. Cho, C. Wolf, M. Jang, A. Sadhanala, R. H. Friend, H. Yang, T.-W. Lee, *Adv. Mater.* **2016**, *28*, 7515.
[35] A. H. Proppe, R. Q. Bermudez, H. Tan, O. Voznyy, S. O. Kelley, E. H. Sargent, *J. Am. Chem. Soc.* **2018**, *140*, 2890.
[36] Y. Mao, B. Sarbajit, S. W. Stanislaus, *J. Am. Chem. Soc.* **2003**, *125*, 15718.
[37] C. C. Stoumpos, D. H. Cao, D. J. Clark, J. Young, J. M. Rondinelli, J. I. Jang, J. T. Hupp, M. G. Kanatzidis, *Chem. Mater.* **2016**, *28*, 2852.
[38] D. Cortecchia, S. Neutzner, A. R. S. Kandada, E. Mosconi, D. Meggiolaro, F. De Angelis, C. Soci, A. Petrozza, *J. Am. Chem. Soc.* **2017**, *139*, 39.
[39] T. Zhang, M. I. Dar, G. Li, F. Xu, N. Guo, M. Grätzel, Y. Zhao, *Sci. Adv.* **2017**, *3*, e1700841.
[40] T. Zhao, C.-C. Chueh, Q. Chen, A. Rajagopal, A. K.-Y. Jen, *ACS Energy Lett.* **2016**, *1*, 757.
[41] D. Bi, C. Yi, J. Luo, J.-D. Décoppet, F. Zhang, S. M. Zakeeruddin, X. Li, A. Hagfeldt, M. Grätzel, *Nat. Energy* **2016**, *1*, 16142.
[42] Y. Zhang, Z. Fei, P. Gao, Y. Lee, F. F. Tirani, R. Scopelliti, Y. Feng, P. J. Dyson, M. K. Nazeeruddin, *Adv. Mater.* **2017**, *29*, 1702157.
[43] G. Xing, N. Mathews, S. Sun, S. S. Lim, Y. M. Lam, M. Grätzel, S. Mhaisalkar, T. C. Sum, *Science* **2013**, *342*, 344.
[44] E. M. Y. Lee, W. A. Tisdale, *J. Phys. Chem. C* **2015**, *119*, 9005.
[45] Q. Dong, Y. Fang, Y. Shao, P. Mulligan, J. Qiu, L. Cao, J. Huang, *Science* **2015**, *347*, 967.
[46] D. W. deQuilettes, S. M. Vorpahl, S. D. Stranks, H. Nagaoka, G. E. Eperon, M. E. Ziffer, H. J. Snaith, D. S. Ginger, *Science* **2015**, *348*, 683.
[47] H. Tan, A. Jain, O. Voznyy, X. Lan, F. P. G. de Arquer, J. Z. Fan, R. Quintero-Bermudez, M. Yuan, B. Zhang, Y. Zhao, F. Fan, P. Li, L. N. Quan, Y. Zhao, Z.-H. Lu, Z. Yang, Sjoerd Hoogland, E. H. Sargent, *Science* **2017**, *355*, 722.
[48] Y. Lin, Y. Bai, Y. Fang, Z. Chen, S. Yang, X. Zheng, S. Tang, Y. Liu, J. Zhao, J. Huang, *J. Phys. Chem. Lett.* **2018**, *9*, 654.

